Check for updates

Boosting the catalytic performance of metalloporphyrin-based covalent organic frameworks *via* coordination engineering for CO₂ and O₂ reduction†

Zhixin Ren, [ID] Ke Gong, Bo Zhao, [ID] Shi-Lu Chen [ID] and Jing Xie [ID] *

Metalloporphyrin-based covalent organic frameworks (Por-COFs) are emerging as electrocatalysts; however, so far experiments have primarily focused on M–N₄-coordinated Por-COFs. A wealth of coordination modified systems with potential catalytic capability remains to be explored. Herein, we report a proof-of-concept computational study on the coordination engineering of Por-COFs as electrocatalysts for reducing CO_2 and O_2. Systematic density functional theory calculations were performed on 15 types of heteroatomic Por-COFs, featuring M–$N_xO_yS_z$ (M = Fe, Co, and Ni; $x + y + z = 4$) centers. Calculations predicted that the Co–N_2O_2-Por-COF is an optimal CO_2-to-CO catalyst candidate (limiting potential $U_L^{CO_2RR} = -0.58$ V) and the Ni–N_2S_2-Por-COF is an optimal O_2-to-H_2O catalyst candidate (overpotential $\eta^{ORR} = 0.46$ V); both heteroatomic-Por-COFs display better catalytic activity and selectivity than their corresponding parent M–N_4-Por-COFs. Electronic structure analysis attributes the enhanced catalytic performance to the additional stabilization, endowed by the heteroatoms, of critical reaction intermediates. Furthermore, feature importance analysis based on machine learning models confirmed that the interplay between the central metal and the coordinated atoms is crucial for catalytic performance. This work predicts new Por-COFs as electrocatalysts for CO_2 and O_2 reduction and showcases the great potential of coordination regulation strategies in designing high-performance COF-based electrocatalysts.

1 Introduction

Covalent organic frameworks (COFs) are emerging electrocatalysts for energy conversion and storage, primarily due to their well-defined active sites, tunable coordination and topology, and accessible pore surfaces.[1–5] COFs are organized by organic knots and covalently connected linkers. Recently, the incorporation of metallo-porphyrin (Por) or phthalocyanine (Pc) knots into COFs has resulted in highly active, selective, and stable catalysts for electrochemical reduction of CO_2 and/or O_2.[6–28] In 2015, the Yaghi group developed the first cobalt porphyrin-based COF (*i.e.*, COF-366-Co), which enables a 26-fold increase in electrochemical CO_2 reduction reaction (CO_2RR) activity compared to the molecular porphyrin catalyst.[6] The Jiang group synthesized the CoPc-PDQ-COF,

which enables a 32-fold increase in CO_2-to-CO activity compared to the molecular phthalocyanine catalyst.[25] In addition, the Co-TEPP-COF/C composite and FePc-BBL-COF displayed high electrocatalytic activity and selectivity for the reduction of O_2 to water.[26,27]

Of note, the abovementioned Por/Pc-based COFs share a M–N_4-coordination centre. Coordination engineering, which alters the N_4-environment to heteroatoms, is an effective strategy to improve the catalytic properties of two-dimensional atomic dispersed transition metal catalysts in N-doped carbon, *i.e.* M–N–C single atom catalysts (SACs).[29–33] For example, Zhao *et al.* designed Ni-based carbon nanosheet SACs with NiN_3S sites and Song *et al.* designed Cu-based carbon support SACs with CuN_3O or $CuCO_3$ sites; all of these catalysts showed high catalytic activity and selectivity for CO production.[34,35] Li *et al.* synthesized an *ortho*-coordinated FeN_2O_2@graphene catalyst and achieved enhanced oxygen reduction reaction (ORR) performance in zinc–air batteries.[36] Wang *et al.* synthesized a carbon-supported Ni-based SAC with N_2O_2 coordination for high-efficiency O_2 reduction to H_2O_2.[37] Theoretically, the performance of graphene-based MS_xN_y (M = Fe, Co, Ni, and Cu)

Key Laboratory of Cluster Science of Ministry of Education, Beijing Key Laboratory of Photoelectronic/Electrophotonic Conversion Materials, School of Chemistry and Chemical Engineering, Beijing Institute of Technology, Beijing, 100081, China. E-mail: jingxie@bit.edu.cn

† Electronic supplementary information (ESI) available. See DOI: https://doi.org/10.1039/d3qm01315d

and FeXY$_i$N$_{3-i}$ (X, Y = B, C, O, P, and S) SACs was investigated, leading to promising catalysts for electrochemical CO$_2$RR or water electrolysis, respectively.[38,39] However, to our knowledge, in experiments, coordination engineering has not been applied in Por/Pc-based COFs yet.

As a matter of fact, molecular heteroatomic porphyrins and metallo-heteroatomic porphyrins complexes have already been successfully synthesized.[40–49] These include singly-substituted cores, such as N$_3$O[41–43] and N$_3$S,[44–47] as well as doubly-substituted cores, such as N$_2$O$_2$,[41] N$_2$S$_2$,[47,48] and N$_2$OS.[49] The embedded central metals include Fe, Co, Ni, Cu, Re, and Ru. In addition, H. Kim *et al.* have shown that Ni coordinated with 21-oxatetraphenylporphyrin (N$_3$O-TPP) becomes highly active toward electrochemical CO$_2$-to-CO reduction, unlike the barely active NiN$_4$–TPP complex.[50] These achievements make us believe that it is possible to synthesize heteroatomic-Por-COFs in the future. Accordingly, we anticipate that the incorporation of O and/or S atoms into the porphyrin unit will change the catalytic properties of the COFs, thus affording a series of new catalysts. Hence, a *priori* theoretical computation is important.

Herein, we present a proof-of-concept computational study on the coordination engineering of Por-COFs for catalysing the reduction of CO$_2$ and O$_2$, highlighting their importance in carbon neutrality and fuel cells. Through systematic periodic density functional theory calculations on M–N$_x$O$_y$S$_z$ coordinated Por-COFs (Fig. 1), where M = Fe, Co, and Ni, we confirmed that coordination engineering is an effective strategy to boost the catalytic performance of Por-COFs. Calculations predict the Co–N$_2$O$_2$-Por-COF to be the optimal catalyst candidate for CO$_2$RR while the Ni–N$_2$O$_2$-Por-COF is optimal for ORR. The essence of enhanced catalytic performance was further investigated through electronic structure analysis and machine learning models. This study provides a fundamental mechanistic understanding of a new group of Por-COF electrocatalysts and identifies several candidates for CO$_2$RR/ORR, thus paving the way toward computation-guided design of potential electrocatalysts.

2 Computational details

2.1 Calculation model setup

The metal-anchored Por-COF shown in Fig. 1a was used as the parent model for coordination engineering. It has been readily synthesized with 5,10,15,20-tetrakis(4-benzaldhyde)porphyrin and *p*-phenylenediamine (PPDA).[17,51] A periodic model of the Por-COF was used for calculations throughout this work. The unit cell of monolayer M–N$_x$O$_y$S$_z$-Por-COFs, containing 60 carbon atoms, 8 nitrogen atoms (or one or two to be substituted with oxygen and/or sulphur atoms), 36 hydrogen atoms, and 1 metal atom, was used. Furthermore, a 20 Å vacuum layer was placed on top of the surface to prevent mirror interactions.

2.2 Density functional theory (DFT) calculation methods

Spin polarized periodic DFT calculations were performed using the Vienna Ab initio Simulation Package (VASP).[52,53] Electron exchange and correction were described using the Perdew–Burke–Ernzerhof (PBE) functional within the generalized gradient approximation (GGA).[54,55] Grimmes's D3 scheme of dispersion correction was included to describe the van der Waals (vdW) interaction.[56] The plane wave basis was employed using the projector augmented wave (PAW) method with a cutoff energy of 520 eV.[57,58] The DFT+U calculations were performed and the corresponding U–J values are listed in Table S1 (ESI†).[59,60] Brillouin zone was sampled using $3 \times 3 \times 1$ and $5 \times 5 \times 1$ k-point grids for geometry optimization and electronic structure calculations, respectively. All atoms were allowed to relax during geometry optimization, and the convergence criteria for force and energy were set to be 10^{-2} eV Å^{-1} and 10^{-5} eV, respectively. A vacuum layer of 20 Å was placed between adjacent layers to prevent interaction. For M = Fe/Co/Ni, different
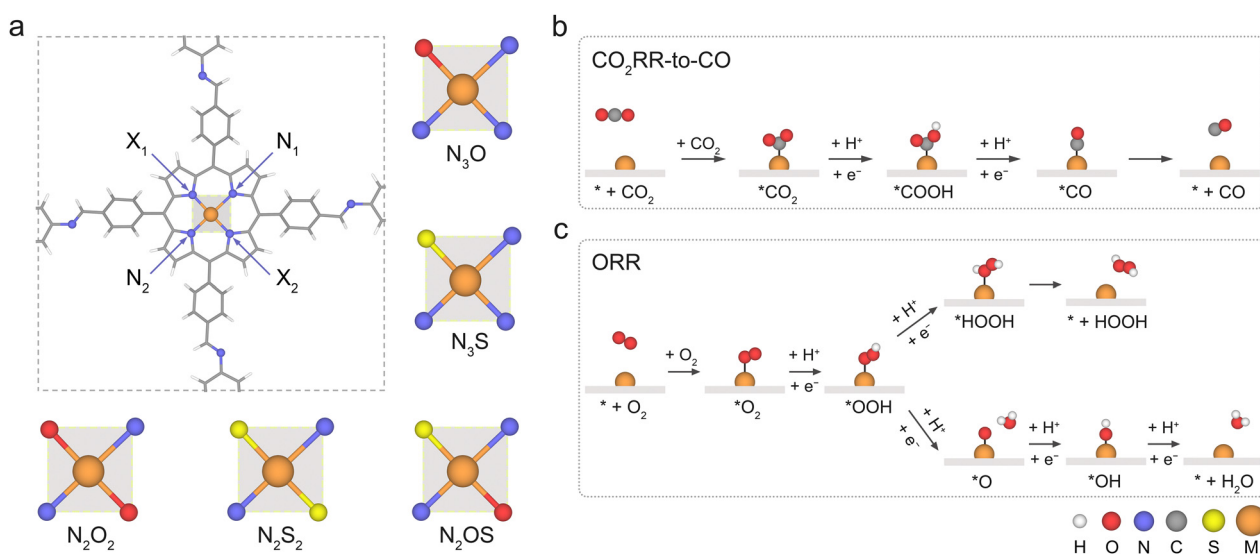

Fig. 1 (a) Unit cell of the M−N$_4$-Por-COF (M = Fe/Co/Ni) considered in this work and the constructed N$_x$O$_y$S$_z$ coordination models. Reaction pathways for (b) CO$_2$RR-to-CO and (c) ORR-to-H$_2$O$_2$ (2e$^-$)/H$_2$O (4e$^-$).

spin states were tested and the discussed data correspond to the most stable structures (Tables S2–S4, ESI†). The implicit solvent model implemented in VASPsol with a dielectric constant of 78.4 was used for the aqueous solution.[61,62]

2.3 Reaction free energy calculation

The computational hydrogen electrode (CHE) model developed by Nørskov *et al.*[63] was applied to obtain the thermodynamic Gibbs free energy change (ΔG) of all elementary reactions:

$$\Delta G = \Delta E + \Delta E_{ZPE} - T\Delta S + \Delta G_U + \Delta G_{pH} \quad (1)$$

where ΔE, ΔE_{ZPE} and ΔS are the difference in electronic energy, zero-point energy correction and entropy between the product and the reactant of each elementary reaction, respectively, and T is set as 298.15 K. E_{ZPE} and ΔS were obtained by calculating the vibrational frequencies for the adsorption intermediates (Tables S5 and S6, ESI†). ΔG_U and ΔG_{pH} represent the free energy corrections caused by the electrode potential (U) and the H$^+$ concentration, respectively. Specifically, $\Delta G_U = -neU$, where n is the number of transferred electrons and U is the applied potential; $\Delta G_{pH} = k_B T \times \ln 10 \times pH$, where k_B is the Boltzmann constant. The pH is set as 0 in this work for convenience, as has been done in most works.[18,38,39,64] The stability of the designed COFs under highly acidic conditions requires further experimental examination, but existing literature supports that certain M-Por-COFs are stable in acidic solutions.[65–67] In a few cases, energy values were computed at pH = 7 for comparison. It is important to note that the relative catalytic capability of the designed COF catalysts remains the same under different pH conditions.

The potential-determining step (PDS) is the step with the largest reaction Gibbs free energy value (ΔG_{max}) among all elementary steps. The limiting potential $\left(U_L^{CO_2RR}\right)$ of CO$_2$RR is defined as $U_L = -\Delta G_{max}/e$. The overpotential (η^{ORR}) of ORR is defined as $\eta = U^0 - U_L$, where U^0 is the equilibrium potential.

2.4 Stability evaluations

The thermodynamic and electrochemical stabilities of Por-COFs were investigated using binding energy (E_b), the difference between adsorption energy and cohesive energy ($E_b - E_{coh}$) and dissolution potential (U_{diss}). E_b measures the binding energy between the metal atom and the substrate,[68] E_{coh} measures the cohesion tendency of isolated metal atom to form the bulk metal,[69,70] U_{diss} measures the ability of active metal atoms to resist dissolution under electrochemical conditions;[71] the related equations are as follows

$$E_b = E_{Por-COF+M} - E_{Por-COF} - E_{single-M} \quad (2)$$

$$E_{coh} = E_{bulk} - n \times E_{single-M} \quad (3)$$

$$U_{diss} = U^\circ_{diss(M,bulk)} - \frac{E_b - E_{coh}}{eN_e} \quad (4)$$

where E_{COF+M}, E_{COF}, $E_{single-M}$ and E_{bulk} are the total energy of the Por-COF with M, the Por-COF without M, the single M atom and the total energy of metal atoms in the most stable bulk

structure, respectively; $U^\circ_{diss(M,bulk)}$ and N_e are the standard dissolution potential of bulk metal and the number of electrons involved in dissolution, respectively. $E_b < 0$, $E_b - E_{coh} < 0$, and $U_{diss} > 0$ indicate that the catalyst has excellent thermodynamic and electrochemical stability. These criteria have been used to evaluate the stability of single atom catalysts in several works.[60,72,73]

The dynamic stability of Co–N$_2$O$_2$, Ni–N$_2$S$_2$-, and Fe–N$_2$OS-Por-COFs was further tested through *ab initio* molecular dynamics (AIMD) simulations using the VASP package. A constant volume/temperature (NVT) ensemble and a Nose–Hoover thermostat were used to maintain the temperature at 300 K. The equation of motion is integrated using the Verlet algorithm method with a timestep of 2 fs, and the total simulation time is 10 ps for each system.

2.5 Machine learning (ML)

All machine learning (ML) predictions were conducted using an open-source Scikit-learn library within the Python3 environment.[74] The optimum parameter values for the three different ML algorithms used in this work, *i.e.*, random forest regression (RFR),[75] gradient boosting regression (GBR),[76,77] and extreme gradient boosting regression (XGBoost),[78] are given in Table S7 (ESI†). Twenty widely recognized features relevant to active center properties were selected as input features for training ML models. All data sources were obtained either from existing databases or through single-step optimization calculations.[79] The input dataset was randomly divided into a training set and a test set in a 4 : 1 ratio. Given the constrained dataset size and potential errors stemming from the segmentation process, a fourfold cross-validation approach was implemented to ensure the model's generalizability. This approach entails the creation of four distinct training and test sets for ML model training and evaluation over four iterations. The optimal algorithm for $U_L^{CO_2RR}$ and η^{ORR} prediction was determined by comparing the average values of root mean square error (RMSE) and coefficient of determination value (R^2 score) across four iterations; then, the best prediction on the test set was recorded for discussion.

3 Results and discussion

As shown in Fig. 1a, the metal-anchored Por-COF with PPDA as a linker was used as the parent model for coordination engineering. Three non-noble transition metal centers were considered: M = Fe, Co, and Ni. The four coordinated N atoms were partially substituted with either O or S atoms, leading to 5 different coordination models: N$_3$O, N$_3$S, *ortho*-N$_2$O$_2$, *ortho*-N$_2$S$_2$, and *ortho*-N$_2$OS. Taking together, a total of 15 types of M–N$_x$O$_y$S$_z$-Por-COFs were designed. The optimized structures (Fig. S1, ESI†) of the porphyrin macrocycles of M–N$_3$O- and M–N$_2$O$_2$-Por-COFs maintain the square-planar geometry, as observed in M–N$_4$-Por-COFs, whereas the substituted S atoms are positioned out of the plane due to their bulkier atom size. The observation of plane distortion caused by the bulkier S

atom has been noted in molecular N_3S-, N_2S_2- and N_2OS-porphyrins,[40,46,49] as well as in M–N–C graphene-based SACs.[80,81]

3.1 Stability and conductivity

The thermodynamic and electrochemical stabilities of heteroatomic Por-COFs were evaluated using binding energy (E_b), the difference between binding energy and cohesive energy ($E_b - E_{coh}$) and dissolution potential (U_{diss}). Calculated values (Fig. 2a–c) suggest that the N_3O-, N_3S and N_2O_2-coordinated Por-COFs, similar to the experimentally synthesized M–N_4-Por-COFs, meet all the stability criteria, i.e., $E_b < 0$, $E_b - E_{coh} < 0$ and $U_{diss} > 0$, meaning that the materials are able to avoid migration and aggregation of metal atoms under actual electrochemical work conditions. However, for the N_2S_2- and N_2OS-coordinated Por-COFs, the values of ($E_b - E_{coh}$) are slightly positive and U_{diss} values are slightly negative, which is likely attributed to the structure deformation introduced by S atoms. Hence, we further tested their dynamic stability using ab initio molecular dynamics (AIMD) simulations at 300 K. Throughout the 10 ps simulation, the systems maintain their integrity with the metal atoms sitting in the center position, confirming their structural stability (Fig. S2, ESI†).

Then, the electrical conductivity of the designed materials was evaluated based on their band gaps (E_g). The E_g values of parent M–N_4-Por-COFs are 1.21, 1.39 and 1.45 eV for M = Fe, Co, and Ni, respectively (Fig. 2d and Fig. S3, ESI†). Such large gaps indicate their poor electron transfer ability, consistent with the limited current densities observed in experiments.[17] Encouragingly, the calculated E_g of heteroatomic Por-COFs decreases greatly, suggesting an improved conductivity. Especially, the calculated band gap of Fe–N_3O-, Fe–N_3S-, Co–N_3S-, Co–N_2O_2-,

Ni–N_2O_2- and Ni–N_2OS-Por-COFs vanishes, thus displaying conductor characteristics.

Accordingly, substituting the N-atom with O/S-atoms in the metal coordination of M–N_4-Por-COFs largely maintains stability and improves conductivity, serving as the foundation of further exploration of catalytic performance.

3.2 Catalytic performance

To investigate the effect of the coordination environment on the catalytic performance of Por-COFs, we studied the electrocatalytic reduction reaction of CO_2 and O_2 in sequence.

3.2.1 Reduction of CO_2 to CO. The conversion of CO_2 to CO is the dominant product of CO_2RR catalysed by Por-COFs,[6–11,15,17–19,22,28,82] so it is the focus of this study. As illustrate in Fig. 1b, the pathway of converting CO_2 to CO catalysed by Por-COFs follows these steps: (1) adsorption of CO_2, (2) formation of carboxylic acid intermediate (*COOH) via the 1st proton-coupled electron transfer (PCET) step, (3) dehydration of *COOH intermediates to form *CO intermediates via the 2nd PCET step, and (4) desorption of CO to regenerate the catalyst.

The first step is the adsorption of CO_2. The absorption strength was slightly changed by substituting the N_4-coordination with $N_xO_yS_z$-coordination, with ΔE_{ads-CO_2} ranging from 0.02 to -0.34 eV (Table S8, ESI†). This is consistent with previous reports.[64] Meanwhile, depending on the coordination type the adsorbed shape of CO_2 on Por-COFs (Fig. S4 and S5, ESI†) can either be linear (for the case of N_4, N_3S, and N_2S_2) or bent (for the case of N_2O_2, N_3O, and N_2OS). For the bent case, the M–C_{*CO_2} bond is as short as 1.96 to 2.17 Å, along with a stretching of the C–O bond by 0.05 to 0.10 Å (ca. 4.3–8.6% elongation).

Then, the following catalytic steps for CO_2-to-CO conversion were computed and are presented in the free energy diagrams
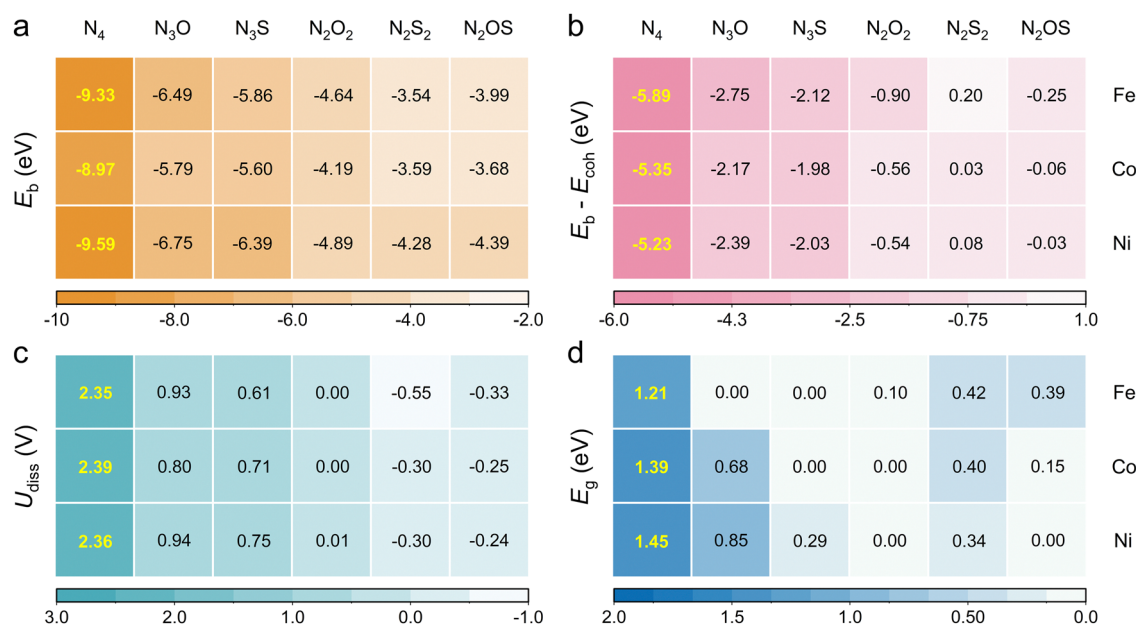

Fig. 2 (a) The binding energy, (b) the difference between binding energy and cohesive energy, (c) the dissolution potential and (d) the band gap of Fe/Co/Ni–$N_xO_yS_z$-Por-COFs.
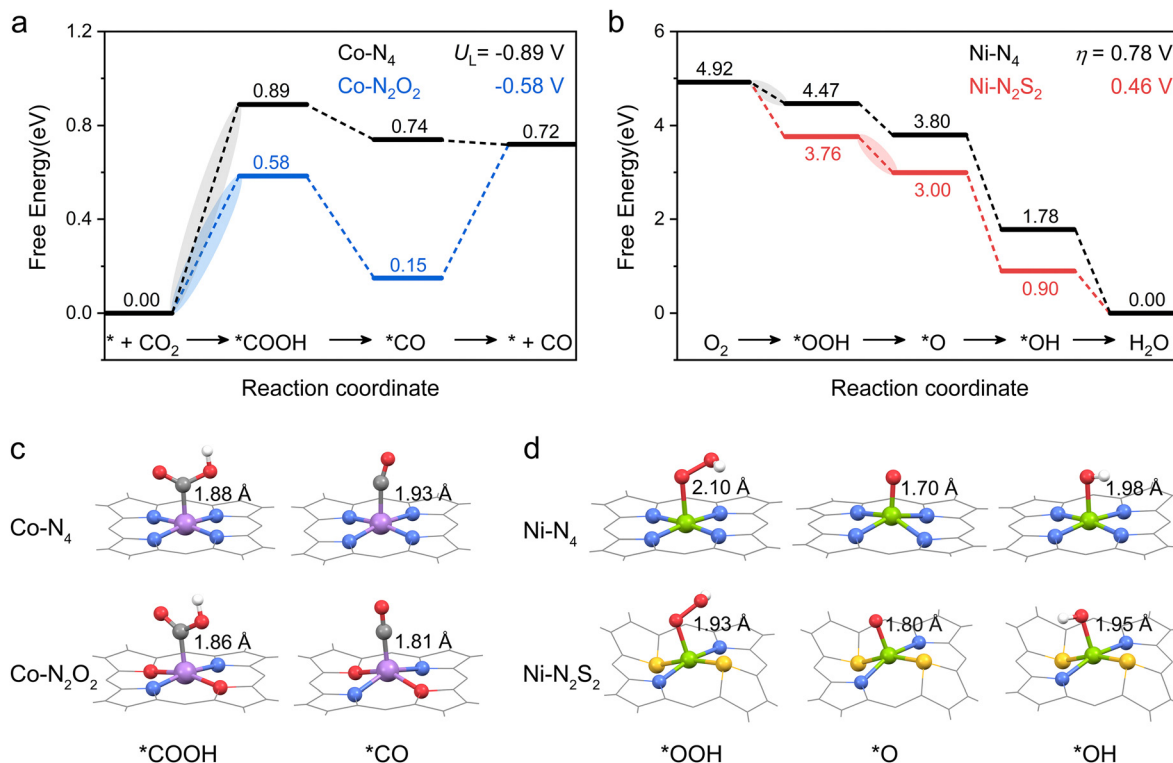
a E_b (eV)

	N₄	N₃O	N₃S	N₂O₂	N₂S₂	N₂OS	
	-9.33	-6.49	-5.86	-4.64	-3.54	-3.99	Fe
	-8.97	-5.79	-5.60	-4.19	-3.59	-3.68	Co
	-9.59	-6.75	-6.39	-4.89	-4.28	-4.39	Ni

-10 -8.0 -6.0 -4.0 -2.0

b $E_b - E_{coh}$ (eV)

	N₄	N₃O	N₃S	N₂O₂	N₂S₂	N₂OS	
	-5.89	-2.75	-2.12	-0.90	0.20	-0.25	Fe
	-5.35	-2.17	-1.98	-0.56	0.03	-0.06	Co
	-5.23	-2.39	-2.03	-0.54	0.08	-0.03	Ni

-6.0 -4.3 -2.5 -0.75 1.0

c U_{diss} (V)

	N₄	N₃O	N₃S	N₂O₂	N₂S₂	N₂OS	
	2.35	0.93	0.61	0.00	-0.55	-0.33	Fe
	2.39	0.80	0.71	0.00	-0.30	-0.25	Co
	2.36	0.94	0.75	0.01	-0.30	-0.24	Ni

3.0 2.0 1.0 0.0 -1.0

d E_g (eV)

	N₄	N₃O	N₃S	N₂O₂	N₂S₂	N₂OS	
	1.21	0.00	0.00	0.10	0.42	0.39	Fe
	1.39	0.68	0.00	0.00	0.40	0.15	Co
	1.45	0.85	0.29	0.00	0.34	0.00	Ni

2.0 1.5 1.0 0.50 0.0

Fig. 3 Free energy diagrams of (a) CO_2RR on $Co-N_4$-and $Co-N_2O_2$-Por-COFs and (b) ORR on $Ni-N_4$-and $Ni-N_2S_2$-Por-COFs. Optimized configurations of (c) *COOH, *CO, and (d) *OOH, *O, *OH intermediates. Color code: Co, purple; Ni, green; C, gray; N, blue; O, red; S, yellow; and H, white. For clarity, the tetraphenyl and *p*-phenylenediamine (PPDA) moieties of $M-N_xO_yS_z$-Por-COFs are not shown. Note: the corresponding free energy diagrams computed at pH = 7 are presented in Fig. S18 (ESI†) for comparison.

(Fig. S6–S8, ESI†). As calculated, the potential determining step (PDS) for all the target $M-N_xO_yS_z$-Por-COFs is the formation of the *COOH intermediate (Fig. 3a and Fig. S6, ESI†). Fig. 4a summarizes the corresponding theoretical limiting potentials U_L. In general, changing the coordination from N_4 to $N_xO_yS_z$ shifts the U_L^{CO2RR} towards the positive direction, meaning an easier reduction and thus higher CO_2-to-CO catalytic activity. This is largely due to the stabilization of the *COOH intermediate, thus lowering the free energy of the PDS ($\Delta G_{*\rightarrow *COOH}$). In comparison, the U_L values of the Co-system are generally less negative than those of the Fe-/Ni-counterparts (Fig. 4a). Among all the designed Fe/Co/Ni-$N_xO_yS_z$-Por-COFs, the $Co-N_2O_2$-Por-COF ($U_L = -0.58$ V) is predicted to be the best CO_2-to-CO catalyst, followed by $Fe-N_2OS$ ($U_L = -0.64$ V), $Fe-N_2O_2$ ($U_L = -0.66$ V) and $Co-N_3O$-Por-COFs ($U_L = -0.67$ V). The above results evidenced that modifying the $M-N_4$ coordination *via* introducing O or/and S atoms is an effective strategy to enhance the CO_2RR catalytic activity of Por-COFs.

In addition, modifying the N_4 coordination also enhances the selectivity of CO_2RR over HER. Unlike the original three $M-N_4$-Por-COFs which exhibit a strong competition between CO_2RR and HER (Fig. 4b and Fig. S9, S10, ESI†), the majority of the designed $M-N_xO_yS_z$-Por-COFs display a distinct preference for CO_2RR. Exceptions are $Ni-N_3O$, $Co-N_3O$, $Co-N_3S$ and $Co-N_2S_2$ systems, which a show slight preference for HER. Such undesired preference can be reversed in practice by adjusting

the pH of the electrolyte or tuning the composition of the electrochemical double layer.[83–85]

Although not the focus of this study, a great portion of spin distribution was observed on the porphyrin ligands, as shown in $Co-N_2O_2$–COOH intermediates (Fig S11, ESI†). This indicates the non-innocent role of the porphyrin ligands, which has been suggested by Liao *et al.*[86–89] This observation gives us a hint that modifying the porphyrin ligand could further tune the catalytic ability of the Por-COFs.

Based on the screening process considering intrinsic stability, catalytic activity, and selectivity, four CO_2-to-CO catalyst candidates are predicted: $Co-N_2O_2$, $Fe-N_2OS$, $Fe-N_2O_2$ and $Co-N_3O$-Por-COFs. Remarkably, all of them display performance comparable to available Por-COFs synthesized through experiments (Fig. S12, ESI†). It is worth noting that these newly designed Por-COFs may yield deep-reduction C1 products (CH_3OH and CH_4), especially when combined with photosensitizers, sacrificial electron donors, or supporting materials.[22,82,87,89–91] These aspects merit further exploration, but we have limited this work to CO_2-to-CO reduction.

In brief, incorporating O/S atoms to modulate the coordination environment of active metals in Fe/Co/Ni-Por-COFs has been proven to be useful for CO_2-to-CO catalyst design. To explore the generality of this coordination modulation strategy, we now redirect our attention to another crucial electroreduction reaction, ORR.
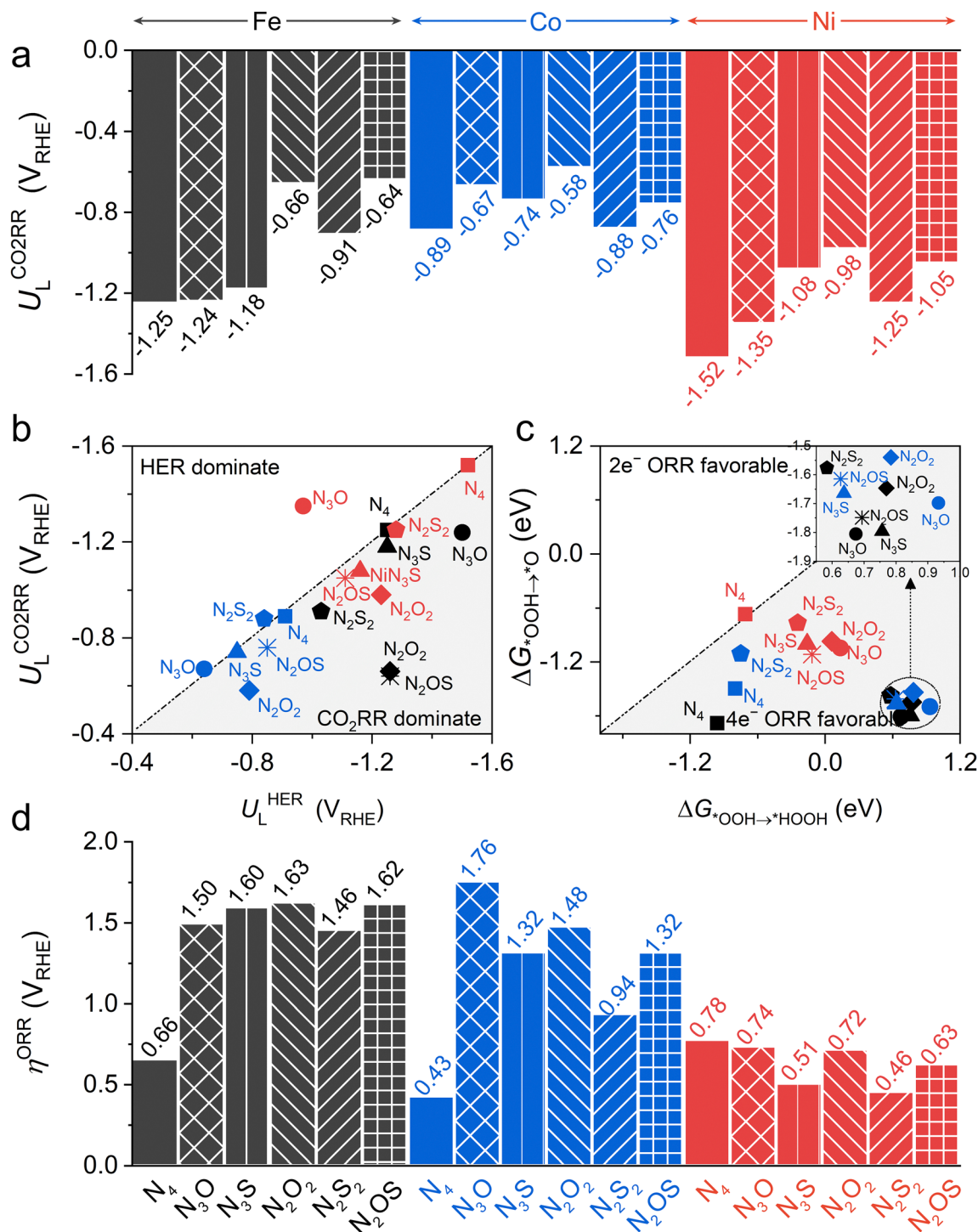
Fig. 4 (a) Limiting potential of CO$_2$RR-to-CO of Fe/Co/Ni–N$_x$O$_y$S$_z$-Por-COFs. (b) Limiting potential of CO$_2$RR-to-CO vs. limiting potential of HER. (c) Gibbs free energy changes ($\Delta G_{*OOH \rightarrow *O}$) of *O formation vs. Gibbs free energy changes ($\Delta G_{*OOH \rightarrow HOOH}$) of HOOH formation. (d) Overpotential of ORR-to-H$_2$O of Fe/Co/Ni–N$_x$O$_y$S$_z$-Por-COFs.

3.2.2 Oxygen reduction reaction. Typically, the catalyzed ORR under acidic conditions can proceed through either a two-electron (2e$^-$) pathway, resulting in the production of H$_2$O$_2$, or a four-electron (4e$^-$) pathway, resulting in the production of H$_2$O. Fig. 1c shows the specific reaction pathways.

The adsorption of O$_2$ is the first step of ORR. In comparison, all the O/S coordinated Por-COFs show stronger adsorption of O$_2$ than the parent M–N$_4$-systems, with the exception of the Ni–N$_2$S$_2$-system. Observing the most stable O$_2$-adsorbed configurations on the M–N$_x$O$_y$S$_z$-Por-COF (Fig. S13–S15, ESI†)

shows that Fe-systems favour a side-on configuration (resembling the Griffiths-type) while Co/Ni-systems, except the Co–N_2OS case, favour an end-on configuration (resembling the Pauling-type). The side-on $*O_2$ structures exhibit a greater O–O bond stretch relative to the free O_2 (over 14% elongation for Fe-systems) than that of end-on $*O_2$ (roughly 10% elongation for Co/Ni-systems), indicating stronger activation of O_2 in the former (Fig. S16 and Table S9, ESI†). The calculated O_2 adsorption energy (ΔE_{ads-O_2}) ranges from −0.18 to −1.58 eV, indicating chemisorption of O_2.

Since the $2e^-$ and $4e^-$ ORR pathways share the first two steps ($* + O_2 \rightarrow *O_2$ and $*O_2 \rightarrow *OOH$) and diverge at the $*OOH$ intermediate, the selectivity is determined by the competition between the free energy difference of $\Delta G_{*OOH \rightarrow *HOOH}$ and $\Delta G_{*OOH \rightarrow *O}$. Fig. 4c shows that all the considered catalysts favour the $4e^-$ ORR pathway over the $2e^-$ ORR pathway, except for the Ni–N_4-system shows similar preference, whose $\Delta G_{*OOH \rightarrow *O}$ is −0.67 eV and $\Delta G_{*OOH \rightarrow *HOOH}$ is −0.71 eV. Hence, we will focus on the $4e^-$ ORR pathway, which converts O_2 to H_2O, in the following discussion.

The effect of changing coordination from N_4 to $N_xO_yS_z$ on $4e^-$ ORR activity is central-metal-dependent: the ORR activity is enhanced when M = Ni, however it is inhibited when M = Fe or Co (Fig. 4d). An ideal $4e^-$ ORR catalyst requires the ΔG of each elementary step to be ~−1.23 eV at zero potential, but normally the differential adsorption/desorption behavior of the intermediates will disrupt this balance and results in overpotentials (η^{ORR}). Specifically, each catalyst has a different PDS for the $4e^-$ ORR (Fig. 3b and Fig. S17, ESI†): 1st step ($* + O_2 \rightarrow *OOH$) for Ni–N_4, Co–N_4, and Co–N_2S_2 system; 2nd step ($*OOH \rightarrow *O$) for the Ni–N_2S_2 system, and 4th step ($*OH \rightarrow *H_2O$) for the rest. Although the parent M–N_4 catalysts have lower η^{ORR} values for Fe–N_4 (0.66 V) and Co–N_4 (0.43 V) than for Ni–N_4 (0.78 V), changing the coordinated environment to $N_xO_yS_z$ only lowers the η^{ORR} of Ni-systems. These heteroatom-coordinated Ni-systems are Ni–N_3O (η^{ORR} = 0.74 V), Ni–N_2O_2 (0.72), Ni–N_2OS (0.63 V), Ni–N_3S (0.51 V) and Ni–N_2S_2 (0.46 V). The increase in η^{ORR} for heteroatom-coordinated Fe/Co-systems is attributed to the excessive strong adsorption of some intermediates (Fig. S19–S21, ESI†). Of note, the parent Co–N_4-catalysts exhibits the lowest η^{ORR} of 0.43 V, followed by the Ni–N_2S_2 (0.46) and Ni–N_3S (0.51) systems. All of them are promising ORR electrocatalyst candidates as compared to the commercial Pt (111) catalyst (η^{ORR} = 0.45 V).[63]

3.3 Activity origin

The above calculations predict that, among the modified Por-COFs, the Co–N_2O_2-Por-COF is the best catalyst candidate for CO_2 reduction and the Ni–N_2S_2-Por-COF is the best candidate for O_2 reduction. To understand the reason behind the improved catalytic performance compared to parent Co–N_4/Ni–N_4-Por-COFs, electronic structure analyses were performed. It has been found that by changing the coordination from N_4 to N_2O_2/N_2S_2, the key intermediates associated with the PDSs were stabilized due to a better match between the orbitals of the central metal and the adsorbed species, thus improving catalytic activity.

In terms of comparison between Co–N_2O_2 and Co–N_4, $*COOH$ serves as the key intermediate for CO_2-to-CO conversion (Fig. 3a). Changing the coordination from N_4 to N_2O_2 increases the orbital overlap between Co's 3d orbitals and the $*COOH$' 2p orbitals, as depicted in Fig. 5a and b. The charge transferred from Co to the COOH-moiety (Fig. 5c and d) increases from 0.15 e^- (Co–N_4) to 0.32 e^- (Co–N_2O_2), and the respective Co−C_{*COOH} bond length decreases from 1.88 to 1.86 Å (Fig. 3c). Hence, the improved matching of critical orbitals leads to the stabilization of the $*COOH$ intermediate, thus lowering the ΔG of step $* + CO_2 \rightarrow *COOH$ (Fig. 3a).

Similarly, when comparing Ni–N_4 and Ni–N_2S_2 for the $4e^-$ ORR, the key intermediate $*OOH$ was stabilized (Fig. 3b). A greater orbital overlap between Ni 3d orbitals and the 2p orbital of the adsorbed species was found as the coordination of Ni shifted from N_4 to N_2S_2 (Fig. 5e, f and Fig. S22, ESI†). The charge transferred from the substrate to intermediates increases from 0.28 e^- to 0.49 e^- for $*OOH$ (Fig. 5g and h), from 0.33 e^- to 0.43 e^- for $*O$ (Fig. S22, ESI†), and from 0.46 e^- to 0.57 e^- for $*OH$. The differential stabilization of these species collectively contributes to the adsorption–desorption equilibrium of reaction intermediates, thus decreasing the overpotential of the Ni–N_2S_2-Por-COF (Fig. 3b).

Overall, the increased catalytic performance of Co–N_2O_2-and Ni–N_2S_2-Por-COFs is attributed to the stabilization of critical
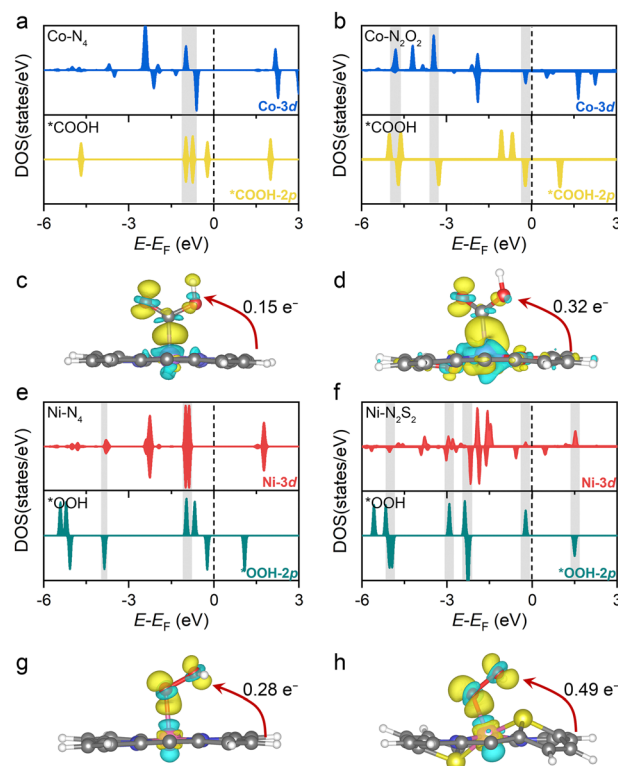

Fig. 5 Projected electronic densities of states (PDOS) and charge density difference (CDD) of (a)–(d) $*COOH$ intermediates adsorbed on Co–N_4- and Co–N_2O_2-Por-COFs, and (e)–(h) $*OOH$ intermediates adsorbed on Ni–N_4- and Ni–N_2S_2-Por-COFs. The cyan/yellow colors indicate the regions of electron loss/gain. Isosurfaces of charge density are set to 0.005 e Å^{-3}. For clarity, the tetraphenyl and the p-phenylenediamine (PPDA) moieties of M–$N_xO_yS_z$-Por-COFs are not shown.

Table 1 Features used for training the ML models

Category	Features	Abbreviation
Properties of central metal	Atomic number	N^{atom}
	Number of valence electron	n_e
	Number of d electron	n_d
	Covalent radius	r^{atom}
	van der Waals radius	r^{vdW}
	Relative mass	m
	Pauling electronegativity	EN
	Electron affinity	EA
	First ionization energy	IE
Properties of coordinated atoms	Number of coordinated N atoms	n_N
	Sum of valence electron count	$\sum n_e$
	Sum of p electron	$\sum n_p$
	Sum of covalent radius	$\sum r^{atom}$
	Sum of van der Waals radius	$\sum r^{vdw}$
	Sum of Pauling electronegativity	$\sum EN$
	The sum of electron affinity	$\sum EA$
DFT calculated bond length	M–X$_1$	d_{M-X1}
	M–X$_2$	d_{M-X2}
	M–N$_1$	d_{M-N1}

intermediates *via* the introduction of heteroatoms into the coordination. Such enhanced effects due to heteroatoms have also been observed in multiple electrocatalysts.[92–94]

3.4 Machine learning (ML)

Furthermore, we used ML to find the intrinsic characteristics that contribute to the differential CO_2RR or ORR performance

of the above Por-COFs. As listed in Table 1, twenty widely recognized features were selected as input features for training the ML models. Numeric values of the features are present in Table S10 (ESI†). Since the size of the sample set is small, 18 in our case (14 in the training set and 4 in the test set), we tried three algorithms: the random forest regression (RFR), gradient boosting regression (GBR), and extreme gradient boosting
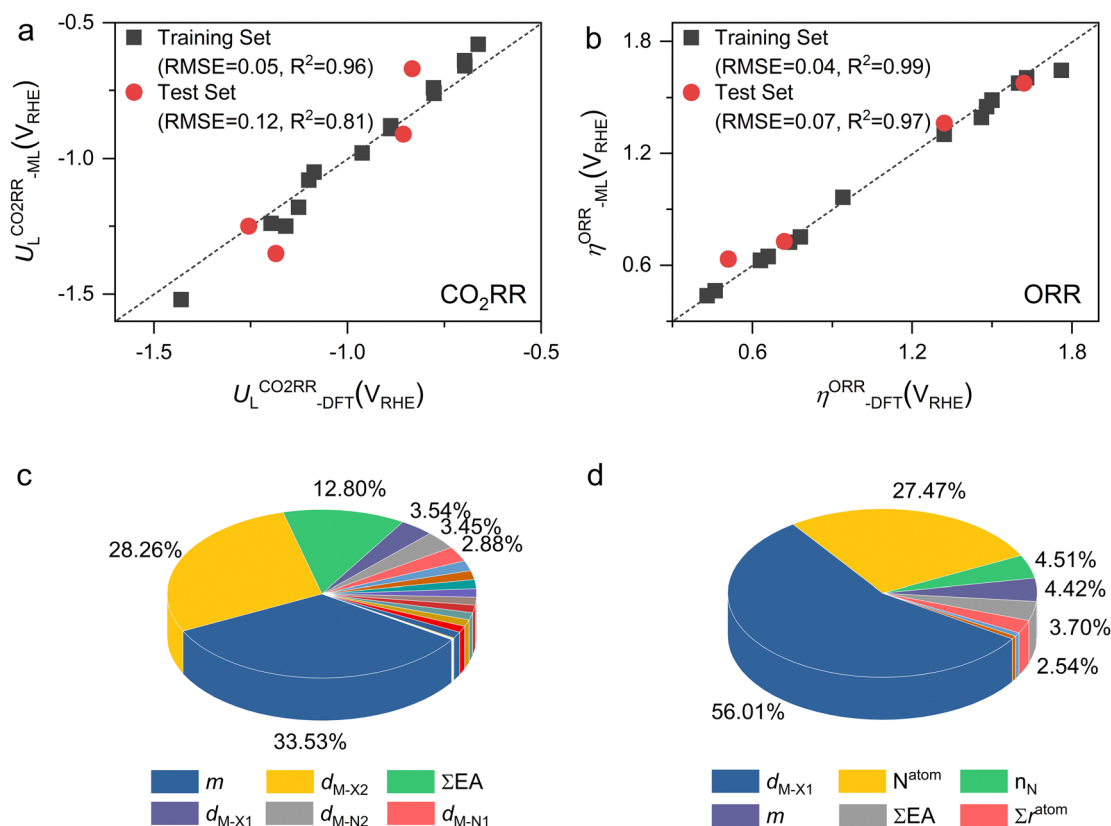

Fig. 6 Comparison between DFT-calculated and ML-predicted values of (a) $U_L^{CO_2RR}$ and (b) η^{ORR}. Feature importance for (c) $U_L^{CO_2RR}$ in the GBR model and (d) η^{ORR} in the XGBoost model.

regression (XGBoost) algorithms. Then, GBR was selected for predicting $U_L^{CO_2RR}$ and XGBoost was selected for predicting η^{ORR}, as these models yield the lowest root mean square error (RMSE) and the highest coefficient of determination value (R^2 score) for the training set (Fig. 6 and Tables S11, 12, ESI†). A good linear correlation was achieved between the DFT-calculated and the ML-predicted values (Table S13, ESI†) of both $U_L^{CO_2RR}$ (Fig. 6a) and η^{ORR} (Fig. 6b). The data of the test set are distributed near the diagonal line, indicating that the trained ML models are capable of predicting the catalytic activity of M-$N_xO_yS_z$-Por-COFs for CO_2RR and ORR, where M = Fe/Co/Ni.

Then, feature importance analysis was performed based on the selected models to evaluate the significance of the features. For $U_L^{CO_2RR}$, the most important features (Fig. 6c) are the relative mass of central metals, m (33.53%); the M–X_2 bond length, d_{M-X2} (28.26%); and the sum of electron affinity of coordination environments, $\sum EA$ (12.80%). Other bond length features, including d_{M-X1}, d_{M-N2}, and d_{M-N1} (each accounts for $\sim$3%), also have some importance. For η^{ORR}, the most crucial features (Fig. 6d) are the M–X_1 bond length, d_{M-X1} (56.01%), and the atomic number of central metals, N^{atom} (27.47%); followed by the number of coordinated N atoms, n_N, (4.51%), the relative mass of central metals, m (4.42%), the sum of electron affinity of coordination environments, $\sum EA$ (3.70%) and the sum of covalent radius of coordination environments, $\sum r^{atom}$ (2.54%). The remaining features contribute insignificantly (Table S14, ESI†). The fact that the important features of CO_2RR and ORR are different is not unexpected, because their inherent mechanisms are different. As a matter of fact, one can see that no single feature overwhelmingly dominates the prediction. Hence the interplay between the central metal and the coordinated atoms is very important for determining the catalytic capability.

We further tested the applicability of the trained model in predicting CO_2RR or ORR catalytic performance of systems beyond the training set, *i.e.*, central metal being Cu or Pt, and coordination atoms including C (refer to ESI† Note S1 for further details). There is a broad agreement on the catalytic order, which is inspiring; nevertheless, the match between ML-predicted and DFT-calculated values is not satisfactory ($\sim$0.3 V error). We anticipate that increasing the sample size and type in the training set would improve the accuracy of the model, and this is currently underway in our group.

4 Conclusions

In summary, by adopting the strategy of substituting N-atoms with O/S-atoms in the metallo-porphyrin unit, our calculations have identified several types of $N_xO_yS_x$-coordinated metallo-Por-COFs as catalyst candidates for CO_2 or O_2 electroreduction. Since current efforts to enhance the catalytic performance of Por-COFs mainly focus on modifying the metal or the length or type of the linker, this study offers an alternative promising strategy: coordination engineering.

Changing the N_4-coordination to $N_xO_yS_z$-coordination (1) improved the conductivity of the M-Por-COFs (M= Fe/Co/Ni), while maintaining their stability; (2) enhanced the CO_2-to-CO reduction catalytic capability and selectivity against the HER in general; and (3) did not alter the preference for the 4e^- ORR in comparison to the 2e^- path, and increased the ORR activity for M = Ni, while hindering it for M = Fe/Co. We predict that the Co–N_2O_2-Por-COF $\left(U_L^{CO_2RR} = -0.58 \text{ V} \right)$ is the best catalyst candidate for CO_2-to-CO reduction and the Ni–N_2S_2-Por-COF (η^{ORR} = 0.46 V) is the best candidate for ORR-to-H_2O reduction. The improved catalytic performance, as compared to their parent M–N_4-system, is attributed to a better orbital match between the central metal and the adsorbed species, leading to the stabilization of the critical intermediate of the potential determining step. Feature importance analysis based on machine leaning models showed that the relative mass of central metals and the bond length between metal and coordinated heteroatoms are the most important intrinsic characteristics for activity prediction.

This study showcases that the coordination engineering is an effective strategy for improving the catalytic performance of Por-based COFs. We envision that this strategy will have broader applications beyond Por-COFs. Although this study presents valuable findings, the mechanisms were solely based on the energetics of stationary points and neglected the kinetics. Further exploration of the detailed mechanisms of the best catalyst candidates is warranted and the impact of pH and explicit solvent molecules shall be taken into account. Besides, although the machine learning model provides information on the weight of important features, the predictability of the model is unsatisfactory. To improve the predictability and transferability of the model, it is necessary to expand the size and diversity of the dataset. Furthermore, the combination of changing the coordination environment and the linkers is also worth exploring.

Author contributions

Zhixin Ren: conceptualization, investigation, methodology, formal analysis, visualization, and writing – original draft. Ke Gong: formal analysis. Bo Zhao: visualization. Shi-Lu Chen: methodology and writing – review and editing. Jing Xie: conceptualization, visualization, supervision, resources, project administration, and writing – review and editing.

Conflicts of interest

The authors declare that they have no conflict of interest.

Acknowledgements

Notes and references

1 A. P. Côté, A. I. Benin, N. W. Ockwig, M. O'Keeffe, A. J. Matzger and O. M. Yaghi, Porous, crystalline, covalent organic frameworks, *Science*, 2005, **310**, 1166–1170.

2 P. J. Waller, F. Gándara and O. M. Yaghi, Chemistry of Covalent Organic Frameworks, *Acc. Chem. Res.*, 2015, **48**, 3053–3063.

3 C. S. Diercks and O. M. Yaghi, The atom, the molecule, and the covalent organic framework, *Science*, 2017, **355**, eaal1585.

4 J. Li, X. Jing, Q. Li, S. Li, X. Gao, X. Feng and B. Wang, Bulk COFs and COF nanosheets for electrochemical energy storage and conversion, *Chem. Soc. Rev.*, 2020, **49**, 3565–3604.

5 Z. Alsudairy, N. Brown, A. Campbell, A. Ambus, B. Brown, K. Smith-Petty and X. Li, Covalent organic frameworks in heterogeneous catalysis: recent advances and future perspective, *Mater. Chem. Front.*, 2023, **7**, 3298–3331.

6 S. Lin, C. S. Diercks, Y.-B. Zhang, N. Kornienko, E. M. Nichols, Y. Zhao, A. R. Paris, D. Kim, P. Yang, O. M. Yaghi and C. J. Chang, Covalent organic frameworks comprising cobalt porphyrins for catalytic CO_2 reduction in water, *Science*, 2015, **349**, 1208–1213.

7 C. S. Diercks, S. Lin, N. Kornienko, E. A. Kapustin, E. M. Nichols, C. Zhu, Y. Zhao, C. J. Chang and O. M. Yaghi, Reticular Electronic Tuning of Porphyrin Active Sites in Covalent Organic Frameworks for Electrocatalytic Carbon Dioxide Reduction, *J. Am. Chem. Soc.*, 2018, **140**, 1116–1122.

8 P. L. Cheung, S. K. Lee and C. P. Kubiak, Facile Solvent-Free Synthesis of Thin Iron Porphyrin COFs on Carbon Cloth Electrodes for CO_2 Reduction, *Chem. Mater.*, 2019, **31**, 1908–1919.

9 Q. Wu, R.-K. Xie, M.-J. Mao, G.-L. Chai, J.-D. Yi, S.-S. Zhao, Y.-B. Huang and R. Cao, Integration of Strong Electron Transporter Tetrathiafulvalene into Metalloporphyrin-Based Covalent Organic Framework for Highly Efficient Electroreduction of CO_2, *ACS Energy Lett.*, 2020, **5**, 1005–1012.

10 H.-J. Zhu, M. Lu, Y.-R. Wang, S.-J. Yao, M. Zhang, Y.-H. Kan, J. Liu, Y. Chen, S.-L. Li and Y.-Q. Lan, Efficient electron transmission in covalent organic framework nanosheets for highly active electrocatalytic carbon dioxide reduction, *Nat. Commun.*, 2020, **11**, 497.

11 S. An, C. Lu, Q. Xu, C. Lian, C. Peng, J. Hu, X. Zhuang and H. Liu, Constructing Catalytic Crown Ether-Based Covalent Organic Frameworks for Electroreduction of CO_2, *ACS Energy Lett.*, 2021, **6**, 3496–3502.

12 M. Chen, H. Li, C. Liu, J. Liu, Y. Feng, A. G. H. Wee and B. Zhang, Porphyrin- and porphyrinoid-based covalent organic frameworks (COFs): From design, synthesis to applications, *Coord. Chem. Rev.*, 2021, **435**, 213778.

13 W. Ji, T.-X. Wang, X. Ding, S. Lei and B.-H. Han, Porphyrin- and phthalocyanine-based porous organic polymers: From synthesis to application, *Coord. Chem. Rev.*, 2021, **439**, 213875.

14 Z. Liang, H.-Y. Wang, H. Zheng, W. Zhang and R. Cao, Porphyrin-based frameworks for oxygen electrocatalysis and catalytic reduction of carbon dioxide, *Chem. Soc. Rev.*, 2021, **50**, 2540–2581.

15 Q. Wu, M.-J. Mao, Q.-J. Wu, J. Liang, Y.-B. Huang and R. Cao, Construction of Donor–Acceptor Heterojunctions in Covalent Organic Framework for Enhanced CO_2 Electroreduction, *Small*, 2021, **17**, 2004933.

16 J.-Y. Yue, Y.-T. Wang, X. Wu, P. Yang, Y. Ma, X.-H. Liu and B. Tang, Two-dimensional porphyrin covalent organic frameworks with tunable catalytic active sites for the oxygen reduction reaction, *Chem. Commun.*, 2021, **57**, 12619–12622.

17 H. Dong, M. Lu, Y. Wang, H.-L. Tang, D. Wu, X. Sun and F.-M. Zhang, Covalently anchoring covalent organic framework on carbon nanotubes for highly efficient electrocatalytic CO_2 reduction, *Appl. Catal., B*, 2022, **303**, 120897.

18 M. Fang, L. Xu, H. Zhang, Y. Zhu and W.-Y. Wong, Metalloporphyrin-Linked Mercurated Graphynes for Ultrastable CO_2 Electroreduction to CO with Nearly 100% Selectivity at a Current Density of 1.2 A cm^{-2}, *J. Am. Chem. Soc.*, 2022, **144**, 15143–15154.

19 T. He, C. Yang, Y. Chen, N. Huang, S. Duan, Z. Zhang, W. Hu and D. Jiang, Bottom-Up Interfacial Design of Covalent Organic Frameworks for Highly Efficient and Selective Electrocatalysis of CO_2, *Adv. Mater.*, 2022, **34**, 2205186.

20 S. Huang, K. Chen and T.-T. Li, Porphyrin and phthalocyanine based covalent organic frameworks for electrocatalysis, *Coord. Chem. Rev.*, 2022, **464**, 214563.

21 M. Liu, S. Liu, C.-X. Cui, Q. Miao, Y. He, X. Li, Q. Xu and G. Zeng, Construction of Catalytic Covalent Organic Frameworks with Redox-Active Sites for the Oxygen Reduction and the Oxygen Evolution Reaction, *Angew. Chem., Int. Ed.*, 2022, **61**, e202213522.

22 Y.-R. Wang, H.-M. Ding, X.-Y. Ma, M. Liu, Y.-L. Yang, Y. Chen, S.-L. Li and Y.-Q. Lan, Imparting CO_2 Electroreduction Auxiliary for Integrated Morphology Tuning and Performance Boosting in a Porphyrin-based Covalent Organic Framework, *Angew. Chem., Int. Ed.*, 2022, **61**, e202114648.

23 S. Bhunia, A. Peña-Duarte, H. Li, H. Li, M. F. Sanad, P. Saha, M. A. Addicoat, K. Sasaki, T. A. Strom, M. J. Yacamán, C. R. Cabrera, R. Seshadri, S. Bhattacharya, J.-L. Brédas and L. Echegoyen, [2,1,3]-Benzothiadiazole-Spaced Co-Porphyrin-Based Covalent Organic Frameworks for O_2 Reduction, *ACS Nano*, 2023, **17**, 3492–3505.

24 Y. Yuan, K.-T. Bang, R. Wang and Y. Kim, Macrocycle-Based Covalent Organic Frameworks, *Adv. Mater.*, 2023, **35**, 2210952.

25 N. Huang, K. H. Lee, Y. Yue, X. Xu, S. Irle, Q. Jiang and D. Jiang, A Stable and Conductive Metallophthalocyanine Framework for Electrocatalytic Carbon Dioxide Reduction in Water, *Angew. Chem., Int. Ed.*, 2020, **59**, 16587–16593.

26 G. Lu, H. Yang, Y. Zhu, T. Huggins, Z. J. Ren, Z. Liu and W. Zhang, Synthesis of a conjugated porous Co(II)

porphyrinylene–ethynylene framework through alkyne metathesis and its catalytic activity study, *J. Mater. Chem. A*, 2015, **3**, 4954–4959.

27 Z. Zhang, W. Wang, X. Wang, L. Zhang, C. Cheng and X. Liu, Ladder-type π-conjugated metallophthalocyanine covalent organic frameworks with boosted oxygen reduction reaction activity and durability for zinc-air batteries, *Chem. Eng. J.*, 2022, **435**, 133872.

28 X. Zhang, Y. Yuan, H. Li, Q. Wu, H. Zhu, Y. Dong, Q. Wu, Y. Huang and R. Cao, Viologen linker as a strong electron-transfer mediator in the covalent organic framework to enhance electrocatalytic CO_2 reduction, *Mater. Chem. Front.*, 2023, **7**, 2661–2670.

29 X. Li, H. Rong, J. Zhang, D. Wang and Y. Li, Modulating the local coordination environment of single-atom catalysts for enhanced catalytic performance, *Nano Res.*, 2020, **13**, 1842–1855.

30 Y. Zhu, J. Sokolowski, X. Song, Y. He, Y. Mei and G. Wu, Engineering Local Coordination Environments of Atomically Dispersed and Heteroatom-Coordinated Single Metal Site Electrocatalysts for Clean Energy-Conversion, *Adv. Energy Mater.*, 2020, **10**, 1902844.

31 W. Xu, H. Tang, H. Gu, H. Xi, P. Wu, B. Liang, Q. Liu and W. Chen, Research progress of asymmetrically coordinated single-atom catalysts for electrocatalytic reactions, *J. Mater. Chem. A*, 2022, **10**, 14732–14746.

32 K. Liu, P. Chen, Z. Sun, W. Chen, Q. Zhou and X. Gao, The atomic interface effect of single atom catalysts for electrochemical hydrogen peroxide production, *Nano Res.*, 2023, **16**, 10724–10741.

33 X. Xie, H. Peng, G. Ma, Z. Lei and Y. Xu, Recent progress in heteroatom doping to modulate the coordination environment of M–N–C catalysts for the oxygen reduction reaction, *Mater. Chem. Front.*, 2023, **7**, 2595–2619.

34 X. Zhao, S. Huang, Z. Chen, C. Lu, S. Han, C. Ke, J. Zhu, J. Zhang, D. Tranca and X. Zhuang, Carbon nanosheets supporting $Ni–N_3S$ single-atom sites for efficient electrocatalytic CO_2 reduction, *Carbon*, 2021, **178**, 488–496.

35 P. Song, B. Hu, D. Zhao, J. Fu, X. Su, W. Feng, K. Yu, S. Liu, J. Zhang and C. Chen, Modulating the Asymmetric Atomic Interface of Copper Single Atoms for Efficient CO_2 Electroreduction, *ACS Nano*, 2023, **17**, 4619–4628.

36 Y. Li, Y. Ding, B. Zhang, Y. Huang, H. Qi, P. Das, L. Zhang, X. Wang, Z.-S. Wu and X. Bao, N,O symmetric double coordination of an unsaturated Fe single-atom confined within a graphene framework for extraordinarily boosting oxygen reduction in Zn–air batteries, *Energy Environ. Sci.*, 2023, **16**, 2629–2636.

37 Y. Wang, R. Shi, L. Shang, G. I. N. Waterhouse, J. Zhao, Q. Zhang, L. Gu and T. Zhang, High-Efficiency Oxygen Reduction to Hydrogen Peroxide Catalyzed by Nickel Single-Atom Catalysts with Tetradentate N_2O_2 Coordination in a Three-Phase Flow Cell, *Angew. Chem., Int. Ed.*, 2020, **59**, 13057–13062.

38 P. Hou, Y. Huang, F. Ma, X. Wei, R. Du, G. Zhu, J. Zhang and M. Wang, S and N coordinated single-atom catalysts for

electrochemical CO_2 reduction with superior activity and selectivity, *Appl. Surf. Sci.*, 2023, **619**, 156747.

39 S. Wang, B. Huang, Y. Dai and W. Wei, Tuning the Coordination Microenvironment of Central Fe Active Site to Boost Water Electrolysis and Oxygen Reduction Activity, *Small*, 2023, **19**, 2205111.

40 T. Chatterjee, V. S. Shetti, R. Sharma and M. Ravikanth, Heteroatom-Containing Porphyrin Analogues, *Chem. Rev.*, 2017, **117**, 3254–3328.

41 P. J. Chmielewski, L. Latos-Grażyński, M. M. Olmstead and A. L. Balch, Nickel Complexes of 21-Oxaporphyrin and 21, 23-Dioxaporphyrin, *Chem. – Eur. J.*, 1997, **3**, 268–278.

42 M. Pawlicki and L. Latos-Grazyński, Iron complexes of 5,10,15,20-tetraphenyl-21-oxaporphyrin, *Inorg. Chem.*, 2002, **41**, 5866–5873.

43 S. Stute, L. Götzke, D. Meyer, M. L. Merroun, P. Rapta, O. Kataeva, W. Seichter, K. Gloe, L. Dunsch and K. Gloe, Molecular Structure, UV/Vis Spectra, and Cyclic Voltammograms of Mn(II), Co(II), and Zn(II) 5,10,15,20-Tetraphenyl-21-oxaporphyrins, *Inorg. Chem.*, 2013, **52**, 1515–1524.

44 J. Lisowski, L. Latos-Grazynski and L. Szterenberg, Nuclear magnetic resonance study of the molecular and electronic structure of nickel(II) tetraphenyl-21-thiaporphyrins, *Inorg. Chem.*, 1992, **31**, 1933–1940.

45 L. Latos-Grazynski, J. Lisowski, P. Chmielewski, M. Grzeszczuk, M. M. Olmstead and A. L. Balch, Palladium complexes of 21-thiaporphyrin: syntheses and characterization, *Inorg. Chem.*, 1994, **33**, 192–197.

46 I. Gupta and M. Ravikanth, Synthesis of meso-furyl porphyrins with N4, N3S, N2S2 and N3O porphyrin cores, *Tetrahedron*, 2003, **59**, 6131–6139.

47 T. Kaur, A. Ghosh, P. Rajakannu and M. Ravikanth, Synthesis and crystal structure of the rhenium(I) tricarbonyl complex of 5,10,15,20-tetra-p-tolyl-21,23-dithiaporphyrin, *Inorg. Chem.*, 2014, **53**, 2355–2357.

48 T. Kaur, W.-Z. Lee and M. Ravikanth, Rhenium(I) Tricarbonyl Complexes of meso-Tetraaryl-21,23-diheteroporphyrins, *Inorg. Chem.*, 2016, **55**, 5305–5311.

49 S. Punidha, N. Agarwal, R. Burai and M. Ravikanth, Synthesis of N3S, N3O, N2S2, N2O2, N2SO and N2OS Porphyrins with One meso-Unsubstituted Carbon, *Eur. J. Org. Chem.*, 2004, 2223–2230.

50 H. Kim, D. Shin, W. Yang, D. H. Won, H.-S. Oh, M. W. Chung, D. Jeong, S. H. Kim, K. H. Chae, J. Y. Ryu, J. Lee, S. J. Cho, J. Seo, H. Kim and C. H. Choi, Identification of Single-Atom Ni Site Active toward Electrochemical CO_2 Conversion to CO, *J. Am. Chem. Soc.*, 2021, **143**, 925–933.

51 Y. Meng, Y. Luo, J.-L. Shi, H. Ding, X. Lang, W. Chen, A. Zheng, J. Sun and C. Wang, 2D and 3D Porphyrinic Covalent Organic Frameworks: The Influence of Dimensionality on Functionality, *Angew. Chem., Int. Ed.*, 2020, **59**, 3624–3629.

52 G. Kresse and J. Hafner, Ab initio molecular dynamics for open-shell transition metals, *Phys. Rev. B: Condens. Matter Mater. Phys.*, 1993, **48**, 13115–13118.

53 G. Kresse and J. Furthmüller, Efficient iterative schemes for ab initio total-energy calculations using a plane-wave

basis set, *Phys. Rev. B: Condens. Matter Mater. Phys.*, 1996, **54**, 11169–11186.

54 J. P. Perdew, K. Burke and M. Ernzerhof, Generalized Gradient Approximation Made Simple, *Phys. Rev. Lett.*, 1996, **77**, 3865–3868.

55 S. Grimme, J. Antony, S. Ehrlich and H. Krieg, A consistent and accurate ab initio parametrization of density functional dispersion correction (DFT-D) for the 94 elements H-Pu, *J. Chem. Phys.*, 2010, **132**, 154104.

56 S. Grimme, S. Ehrlich and L. Goerigk, Effect of the damping function in dispersion corrected density functional theory, *J. Comput. Chem.*, 2011, **32**, 1456–1465.

57 P. E. Blöchl, Projector augmented-wave method, *Phys. Rev. B: Condens. Matter Mater. Phys.*, 1994, **50**, 17953–17979.

58 G. Kresse and D. Joubert, From ultrasoft pseudopotentials to the projector augmented-wave method, *Phys. Rev. B: Condens. Matter Mater. Phys.*, 1999, **59**, 1758–1775.

59 S. L. Dudarev, G. A. Botton, S. Y. Savrasov, C. J. Humphreys and A. P. Sutton, Electron-energy-loss spectra and the structural stability of nickel oxide: An LSDA + U study, *Phys. Rev. B: Condens. Matter Mater. Phys.*, 1998, **57**, 1505–1509.

60 H. Xu, D. Cheng, D. Cao and X. C. Zeng, A universal principle for a rational design of single-atom electrocatalysts, *Nat. Catal.*, 2018, **1**, 339–348.

61 K. Mathew, R. Sundararaman, K. Letchworth-Weaver, T. A. Arias and R. G. Hennig, Implicit solvation model for density-functional study of nanocrystal surfaces and reaction pathways, *J. Chem. Phys.*, 2014, **140**, 084106.

62 K. Mathew, V. S. C. Kolluru, S. Mula, S. N. Steinmann and R. G. Hennig, Implicit self-consistent electrolyte model in plane-wave density-functional theory, *J. Chem. Phys.*, 2019, **151**, 234101.

63 J. K. Nørskov, J. Rossmeisl, A. Logadottir, L. Lindqvist, J. R. Kitchin, T. Bligaard and H. Jónsson, Origin of the Overpotential for Oxygen Reduction at a Fuel-Cell Cathode, *J. Phys. Chem. B*, 2004, **108**, 17886–17892.

64 S. Cao, S. Wei, X. Wei, S. Zhou, H. Chen, Y. Hu, Z. Wang, S. Liu, W. Guo and X. Lu, Can N, S Cocoordination Promote Single Atom Catalyst Performance in CO₂RR? Fe–N₂S₂ Porphyrin versus Fe–N₄ Porphyrin, *Small*, 2021, **17**, 2100949.

65 A. Nagai, X. Chen, X. Feng, X. Ding, Z. Guo and D. Jiang, A Squaraine-Linked Mesoporous Covalent Organic Framework, *Angew. Chem., Int. Ed.*, 2013, **52**, 3770–3774.

66 C. Liu, H. Li, F. Liu, J. Chen, Z. Yu, Z. Yuan, C. Wang, H. Zheng, G. Henkelman, L. Wei and Y. Chen, Intrinsic Activity of Metal Centers in Metal-Nitrogen-Carbon Single-Atom Catalysts for Hydrogen Peroxide Synthesis, *J. Am. Chem. Soc.*, 2020, **142**, 21861–21871.

67 J.-D. Yi, R. Xu, G.-L. Chai, T. Zhang, K. Zang, B. Nan, H. Lin, Y.-L. Liang, J. Lv, J. Luo, R. Si, Y.-B. Huang and R. Cao, Cobalt single-atoms anchored on porphyrinic triazine-based frameworks as bifunctional electrocatalysts for oxygen reduction and hydrogen evolution reactions, *J. Mater. Chem. A*, 2019, **7**, 1252.

68 S. Back, J. Lim, N. Kim, Y. Kim and Y. Jung, Single-atom catalysts for CO₂ electroreduction with significant activity and selectivity improvements, *Chem. Sci.*, 2017, **8**, 1090–1096.

69 Y. Su, L. Zhang, Y. Wang, J. Liu, V. Muravev, K. Alexopoulos, I. A. W. Filot, D. G. Vlachos and E. J. M. Hensen, Stability of heterogeneous single-atom catalysts: a scaling law mapping thermodynamics to kinetics, *npj Comput. Mater.*, 2020, **6**, 144.

70 M. Ha, D. Y. Kim, M. Umer, V. Gladkikh, C. W. Myung and K. S. Kim, Tuning metal single atoms embedded in NₓCᵧ moieties toward high-performance electrocatalysis, *Energy Environ. Sci.*, 2021, **14**, 3455–3468.

71 J. Greeley and J. K. Nørskov, Electrochemical dissolution of surface alloys in acids: Thermodynamic trends from first-principles calculations, *Electrochim. Acta*, 2007, **52**, 5829–5836.

72 C. Fang, J. Zhou, L. Zhang, W. Wan, Y. Ding and X. Sun, Synergy of dual-atom catalysts deviated from the scaling relationship for oxygen evolution reaction, *Nat. Commun.*, 2023, **14**, 4449.

73 X. Guo, S. Zhang, L. Kou, C. Yam, T. Frauenheim, Z. Chen and S. Huang, Data-driven pursuit of electrochemically stable 2D materials with basal plane activity toward oxygen electrocatalysis, *Energy Environ. Sci.*, 2023, **16**, 5003–5018.

74 F. Pedregosa, G. Varoquaux, A. Gramfort, V. Michel, B. Thirion, O. Grisel, M. Blondel, P. Prettenhofer, R. Weiss, V. Dubourg, J. Vanderplas, A. Passos, D. Cournapeau, M. Brucher, M. Perrot and É. Duchesnay, Scikit-learn: Machine Learning in Python, *J. Mach. Learn. Res.*, 2011, **12**, 2825–2830.

75 L. Breiman, Random Forests, *Mach. Learn.*, 2001, **45**, 5–32.

76 J. H. Friedman, Greedy function approximation: A gradient boosting machine, *Ann. Stat.*, 2001, **29**, 1189–1232.

77 J. H. Friedman, Stochastic gradient boosting, *Comput. Stat. Data Anal.*, 2002, **38**, 367–378.

78 T. G. Dietterich, Approximate Statistical Tests for Comparing Supervised Classification Learning Algorithms, *Neural Comput.*, 1998, **10**, 1895–1923.

79 H. Mai, T. C. Le, D. Chen, D. A. Winkler and R. A. Caruso, Machine Learning for Electrocatalyst and Photocatalyst Design and Discovery, *Chem. Rev.*, 2022, **122**, 13478–13515.

80 Z. Jin, D. Jiao, Y. Dong, L. Liu, J. Fan, M. Gong, X. Ma, Y. Wang, W. Zhang, L. Zhang, Z. G. Yu, D. Voiry, W. Zheng and X. Cui, Boosting Electrocatalytic Carbon Dioxide Reduction via Self-Relaxation of Asymmetric Coordination in Fe-based Single Atom Catalyst, *Angew. Chem., Int. Ed.*, 2023, e202318246.

81 H. Jia, A. Nandy, M. Liu and H. J. Kulik, Modeling the roles of rigidity and dopants in single-atom methane-to-methanol catalysts, *J. Mater. Chem. A*, 2022, **10**, 6193–6203.

82 Z. Ren, B. Zhao and J. Xie, Designing N-Confused Metalloporphyrin-Based Covalent Organic Frameworks for Enhanced Electrocatalytic Carbon Dioxide Reduction, *Small*, 2023, **19**, 2301818.

83 A. S. Hall, Y. Yoon, A. Wuttig and Y. Surendranath, Mesostructure-Induced Selectivity in CO₂ Reduction Catalysis, *J. Am. Chem. Soc.*, 2015, **137**, 14834–14837.

84 X.-Q. Li, G.-Y. Duan, J.-W. Chen, L.-J. Han, S.-J. Zhang and B.-H. Xu, Regulating electrochemical CO_2RR selectivity at industrial current densities by structuring copper@poly-(ionic liquid) interface, *Appl. Catal., B*, 2021, **297**, 120471.

85 S. Banerjee, C. S. Gerke and V. S. Thoi, Guiding CO_2RR Selectivity by Compositional Tuning in the Electrochemical Double Layer, *Acc. Chem. Res.*, 2022, **55**, 504–515.

86 Y.-Q. Zhang, J.-Y. Chen, P. E. M. Siegbahn and R.-Z. Liao, Harnessing Noninnocent Porphyrin Ligand to Circumvent Fe-Hydride Formation in the Selective Fe-Catalyzed CO_2 Reduction in Aqueous Solution, *ACS Catal.*, 2020, **10**, 6332–6345.

87 L.-L. Shi, M. Li, B. You and R.-Z. Liao, Theoretical Study on the Electro-Reduction of Carbon Dioxide to Methanol Catalyzed by Cobalt Phthalocyanine, *Inorg. Chem.*, 2022, **61**, 16549–16564.

88 Y.-C. Cao, L.-L. Shi, M. Li, B. You and R.-Z. Liao, Deciphering the Selectivity of the Electrochemical CO_2 Reduction to CO by a Cobalt Porphyrin Catalyst in Neutral Aqueous Solution: Insights from DFT Calculations, *ChemistryOpen*, 2023, **12**, e202200254.

89 J.-Y. Chen, M. Li and R.-Z. Liao, Mechanistic Insights into Photochemical CO_2 Reduction to CH_4 by a Molecular Iron−Porphyrin Catalyst, *Inorg. Chem.*, 2023, **62**, 9400–9417.

90 H. Rao, L. C. Schmidt, J. Bonin and M. Robert, Visible-light-driven methane formation from CO_2 with a molecular iron catalyst, *Nature*, 2017, **548**, 74–77.

91 Y. Wu, Z. Jiang, X. Lu, Y. Liang and H. Wang, Domino electroreduction of CO_2 to methanol on a molecular catalyst, *Nature*, 2019, **575**, 639–642.

92 X. Li, H. Zhang, Q. Hu, W. Zhou, J. Shao, X. Jiang, C. Feng, H. Yang and C. He, Unlocking the Transition of Electrochemical Water Oxidation Mechanism Induced by Heteroatom Doping, *Angew. Chem., Int. Ed.*, 2023, **62**, e202309732.

93 C. Feng, M. Lv, J. Shao, H. Wu, W. Zhou, S. Qi, C. Deng, X. Chai, H. Yang, Q. Hu and C. He, Lattice Strain Engineering of Ni_2P Enables Efficient Catalytic Hydrazine Oxidation-Assisted Hydrogen Production, *Adv. Mater.*, 2023, **35**, 2305598.

94 Q. Hu, K. Gao, X. Wang, H. Zheng, J. Cao, L. Mi, Q. Huo, H. Yang, J. Liu and C. He, Subnanometric Ru clusters with upshifted D band center improve performance for alkaline hydrogen evolution reaction, *Nat. Commun.*, 2022, **13**, 3958.